Optimization of the thermoelectric properties of $SnSe_2$ using first principle calculations

Sree Sourav Das[1], Md. Golam Rosul[2] and Mona Zebarjadi[1,3*]

[1]Department of Electrical and Computer Engineering, University of Virginia, Charlottesville, VA 22904, United States

[2]Department of Engineering, Sweet Briar College, Sweet Briar, VA 24595, United States

[3]Department of Materials Science and Engineering, University of Virginia, Charlottesville, VA 22904, United States

[*]Corresponding author: m.zebarjadi@virginia.edu

Abstract:

We present a first principle framework to study the electronic properties of $SnSe_2$, a potentially good layered thermoelectric material. We use density functional theory and solutions of the Boltzmann transport equation under relaxation time approximation including electron-phonon and ionized impurity interactions to calculate the thermoelectric power factor where electron-phonon scattering is computed using the PERTUBO package and the modified Brooks-Herring approach is used to model the ionized impurity scattering. We study the temperature-dependent transport properties at different carrier concentrations with and without the inclusion of van der Waals interactions. The inclusion of van der Waals interactions increases the electron-phonon scattering but total relaxation time is mostly dominated by ionized impurity scattering at high concentration levels. We first validate our theory by comparing the results to available experimental data and then optimize the thermoelectric performance of $SnSe_2$ as a function of temperature and carrier concentration. The optimized power factor times temperature happens at a carrier concentration of 4×10^{19} cm^{-3} and reaches a maximum value of 0.49 $Wm^{-1}K^{-1}$ at 523 K in the in-plane direction and 0.185 $Wm^{-1}K^{-1}$ at 700 K in the cross-plane direction. Finally, the lattice thermal conductivity is

evaluated using Callaway's model. Our optimized model shows the highest ZT value of 1.1 at 950 K originating in the ultra-low thermal conductivity across the $SnSe_2$ layers.

Introduction

Climate change and energy security are major concerns for a future sustainable society [1,2]. More than 60% of the energy generated in our power plants is wasted in the form of heat. The recovery of this waste heat can play a major role in mitigating the worldwide clean energy shortage. Among possible solutions for waste heat recovery are solid-state thermoelectric modules which can convert heat directly into electricity, based on the Seebeck effect [1,3–10]. In addition to using a clean and abundant energy resource, thermoelectric power generators have several other advantages. They have no moving parts, do not use harmful chemicals, have a quiet operation, and have low maintenance requirements [11–13]. Besides power generation and refrigeration capability, thermoelectric materials are now being considered in active cooling applications [14,15]. Despite the benefits of using thermoelectric modules, their popularity in the market remains relatively low [16] due to their low efficiency, high cost, and in some cases the usage of toxic elements and mechanical instability at high temperatures.

The thermoelectric performance is defined by a dimensionless figure of merit, $ZT = \frac{S^2\sigma T}{\kappa}$, where S, σ, T, and κ represent the Seebeck coefficient, electrical conductivity, temperature, and total thermal conductivity (electronic contribution: κ_{el}+ lattice contribution: κ_{latt}), respectively [12]. It is evident from the above relation that high-performance thermoelectrics need to have a high-power factor ($S^2\sigma$) and low thermal conductivity. However, it is difficult to control these parameters independently due to their complex interrelationships. There are some well-established ways to improve ZT for example by optimizing carrier concentration and mobility which results in

enhanced power factor (PF) or by suppressing the lattice thermal conductivity by introducing scattering centers [13,17–19].

Two-dimensional layered materials such as transition metal dichalcogenides (TMDCs) are promising candidates for thermoelectric applications [20–24] and have unique electronic and thermal transport properties [25]. In layered structure materials, strong covalent bondings exist within each layer and weak van der Waals interactions between them. Because of the weak van der Waals interactions, layered materials possess low thermal conductivity along the cross-plane direction, making them promising thermoelectric materials.

Tin diselenide ($SnSe_2$) has a layered hexagonal CdI_2-type structure [25] and offers several advantages including non-toxicity and low cost but it was overlooked for a long time [16,26]. In this paper, we use first-principles calculations and Boltzmann transport theory to examine the doping and temperature dependence of TE properties of $SnSe_2$. To accurately describe the thermoelectric properties of $SnSe_2$, we use energy-dependent relaxation times including electron-phonon and ionized impurity scatterings in transport calculations. Until now, very few theoretical studies have been performed on this material but they are incomplete as they either use constant relaxation time approximation e.g. employing BoltzTrap code [27], or single parabolic band (SPB) model to predict TE properties of $SnSe_2$ which prevents their formalism to accurately describe and predict the experimental TE properties of $SnSe_2$ [28,29].

Sun et. al [28] used first-principles band structure but constant relaxation times approximation (CRTA) for the transport calculation of $SnSe_2$. They derived a constant value of τ at different temperatures by fitting the electrical conductivities with experimental data. This assumption makes the total transport calculations fast and simple but does not have a predictive power. In practice, τ is not a constant value and is a function of band-structure, energy, temperature, and doping

concentration. Using a constant value of τ can lead to misleading results. For instance, Sun's model [28] predicted a larger ZT in the in-plane direction whereas experimental results suggest that ZT is higher along the cross-plane direction for single crystal samples [25,30]. The discrepancies between theoretical and experimental values also originated from the incorrect modeling of lattice thermal conductivity. In Ref. 26 Cahill's model [31] was used which is only applicable to disorder systems and not to $SnSe_2$. The thermal conductivity of SnSe2 at above room temperature is dominated by three-phonon processes and drops with $(\frac{1}{T})$ which is not the case for disorder systems. Later, Ding et. al [29] used a single parabolic band (SPB) model and only considered the acoustic phonon scattering in the system for electron relaxation time approximation. However, the phonon dispersion of $SnSe_2$ reveals that modeling with only deformation potential cannot describe the detailed nature of the scattering mechanism. Wang et. al [32] and Saeed et. al [33] reported that optical phonons play a significant role in transport for $SnSe_2$ or related phases. Alongside optical phonon scattering, ionized impurity scattering is also a dominant one for doped semiconductors [34]. Therefore, the SPB model with only acoustic modes could lead to the wrong prediction of the relaxation times, especially along the cross-plane direction. Thus, it is necessary to develop a more accurate model including all dominant scattering events to predict the experimental thermoelectric properties of $SnSe_2$. In this work, we develop a first principles-based method incorporating electron-phonon scattering (including acoustic and optical branches) and ionized impurity scattering to match the experimental transport properties of bulk $SnSe_2$ in the in-plane and cross-plane direction without and with van der Waals interactions. The electrical conductivity and Seebeck coefficient are calculated by solving the linearized BTE under energy-dependent relaxation time approximation. The band structure and the electron-phonon scattering rates are obtained using the first principle calculations. The ionized impurity scattering is evaluated using a

modified Brooks-Herring approach [35]. The lattice thermal conductivity is evaluated using the Callaway model as this approach has successfully been applied to predict the κ values for semiconductors [36,37]. The results are in close agreement with the experimental values. Finally, we use our developed method to optimize power factor times temperature with respect to temperature and carrier concentration to obtain optimum temperature and doping concentration for high power factor. Our results may serve as a guide on how to optimize the thermoelectric properties of $SnSe_2$ and similar compounds.

Computational Details:

$SnSe_2$ crystallizes in a layered hexagonal structure with P-3m1 space group and 3 atoms in the unit cell [38]. First-principles calculations are carried out using the density functional theory (DFT) and density functional perturbation theory (DFPT) as implemented in QUANTUM ESPRESSO package [39]. The norm-conserving pseudopotentials [40] with Perdew-Zunger (LDA) [41] exchange-correlation functional is used. The interlayer interactions in $SnSe_2$ arise from weak van der Waals force between Se and Sn atoms in the out-of-plane direction. To capture weak interactions between layers, we use the non-local van der Waals DFT functional (vdW-DF2) [42]. The atomic structure of the crystals is determined by optimizing the atomic positions using the conjugate-gradient method [43] and BFGS quasi-newton algorithm [44] with a force convergence criterion of 10^{-3} Ry/Bohr. A kinetic energy cutoff of 40 Ry and Monkhorst-Pack k-point mesh of 12×12×6 is employed in the atomic and electronic structure calculations. This choice of k-point grid and energy cutoff is chosen such that the maximum force on each atom is less than 4×10^{-3} Ry/Bohr. The obtained lattice structure of hexagonal $SnSe_2$ was 3.81 Å and c=6.137 Å and these values reasonably match the experimentally reported values [30,38]. The dynamical matrix is computed on a 4×4×3 q-point mesh in the phonon calculations. The phonon modes and frequencies at other general k-points are then

computed by Fourier transformation of the dynamical matrix in reciprocal space. The relaxation times (RT) arising from electron-phonon scattering are calculated using the PERTURBO package [45] which utilizes the Wannier interpolation scheme [46]. PERTURBO interpolates the electron-phonon coupling matrices as well as electron and phonon eigenvalues from a coarse grid to a fine grid (40 ×40×40). Details of electron-phonon matrix calculations in PERTURBO are discussed elsewhere [45]. In Wannier interpolation, projections of four sp^3 orbitals centered on each Se and Sn atom are used for the Wannierization [47] of a total of 12 bands. We calculate the ionized impurity scattering rates using a modified Brooks-Herring approach for strongly screened Coulomb potential [35]. The impurity scattering rate is given by,

$$\frac{1}{\tau} = \frac{\pi(N_I/Z)}{\hbar}\left(\frac{q^2 L_D^2}{\varepsilon_0 \varepsilon_r}\right)^2 g(E) \qquad (i)$$

Where $g(E)$ is the density of states, ħ is the reduced Plank constant, ε_r is the relative permittivity, ε_0 is the permittivity of free space, N_I is the impurity carrier concentration, q is the electronic charge, and Z is the charge of the vacancy/impurity atoms. L_D is the screening length and is given by,

$$\frac{1}{L_D^2} = \frac{q^2}{\varepsilon}\int g(E)\frac{\partial f}{\partial E}dE \qquad (ii)$$

where f is the Fermi-Dirac distribution function

Our focus in this paper is the accurate calculation of the thermoelectric power factor, for which we use the first principles as discussed above. However, to be able to comment on the thermoelectric figure of merit, we also need to calculate the thermal conductivity. For this part, we choose a phenomenological approach, and we estimate the thermal conductivity using Callaway's model,

$$\kappa = \frac{k_B}{2\pi^2 c}(I_1 + \beta I_2) \qquad (iii)$$

Where,

$$I_1 = \int_0^{\omega_D} \tau_c \frac{\hbar^2\omega^2}{k_B^2T^2} \frac{e^{\frac{\hbar\omega}{k_BT}}\omega^2}{(e^{\frac{\hbar\omega}{k_BT}}-1)^2} d\omega \qquad (iii)$$

$$I_2 = \int_0^{\omega_D} \frac{\tau_c}{\tau_N} \frac{\hbar^2\omega^2}{k_B^2T^2} \frac{e^{\frac{\hbar\omega}{k_BT}}\omega^2}{(e^{\frac{\hbar\omega}{k_BT}}-1)^2} d\omega \qquad (iv)$$

$$\beta = \frac{\int_0^{\frac{\theta}{T}} \frac{\tau_c}{\tau_N} \frac{e^x x^4}{(e^x-1)^2} d\omega}{\int_0^{\frac{\theta}{T}} (1-\frac{\tau_c}{\tau_N}) \frac{1}{\tau_N} \frac{e^x x^4}{(e^x-1)^2} d\omega}; x = \frac{\hbar\omega}{k_BT} \qquad (v)$$

Scattering time is given by,

$$\tau_c = (\tau_B^{-1} + \tau_N^{-1} + \tau_P^{-1} + \tau_u^{-1})^{-1}$$

$$\tau_c = \left(cL^{-1} + B_1T^3\omega^2 + A\omega^4 + e^{-\frac{\theta}{\alpha T}}T^3\omega^2\right)^{-1} \qquad (vi)$$

Where the total relaxation time, τ_c, is calculated from Matthiessen's rule and by the combination of boundary scattering τ_B, normal three-phonon process τ_N, impurity scattering τ_p, and Umklapp relaxation times, τ_u . A and B_1 are the fitting parameters and α is a constant characteristic of the vibrational spectrum of the material, ω_D and θ are the Debye frequency and temperature, respectively. k_B denotes the Boltzmann constant and c is the sound velocity.

Results and Discussion:

The electronic band structure, electronic density of states (DOS), and phonon dispersion of bulk $SnSe_2$ with and without van der Waals interaction are shown in Figure 1(a-c). In Figure 1(a), the DFT band structure is plotted. The conduction band minimum (CBM) of $SnSe_2$ lies at the L-point and the valence band maximum (VBM) lies along the Γ-M direction in the Brillouin zone denoting the indirect bandgap of $SnSe_2$ [29,48,49]. The conduction band is highly dispersive along Γ-M or Γ-K

directions (in-plane directions) than in the Γ-A direction (cross-plane direction) indicating lower electron effective mass along in-plane directions. The inclusion of van der Waals (vdW) interactions has minimal effects on the electronic band structure. The DFT band structure was then interpolated using the maximally localized Wannier function [47]. The obtained DFT bands and the interpolated bands by Wannier functions [46,47] show very good agreement (see Supplementary Information Figure S1). The obtained band structure from LDA approximation was also compared with PBE functional, G_0W_0 approximation, and HSE hybrid functionals [48]. Although G_0W_0 and HSE bandgaps are closer to the experimental bandgap, there is no change in the curvature of the bands except for the shift in bandgap compared to PBE. The validity of LDA approximation is discussed in Supplementary Information Figure S2. It is well known that LDA functionals underestimate the bandgap for most insulators and semiconductors and so, we have shifted the conduction bands during Wannier to PERTURBO interpolation and obtained a band-gap of 0.95 eV which closely matches the experimental values of 0.97 eV [38].

Phonon dispersion of bulk $SnSe_2$ was calculated and plotted in Figure 1(c). The unit cell of hexagonal $SnSe_2$ has three atoms. As a result, there are nine phonon modes at each k-point but in Γ-A and H-K directions, the out-of-plane vibrational mode ZA is degenerated with the TA branch and only LA and TA branches are visible [29]. Overall, our results are in good agreement with the experimental data obtained by the inelastic neutron scattering method (see Supplementary Information Figure S2)[50].

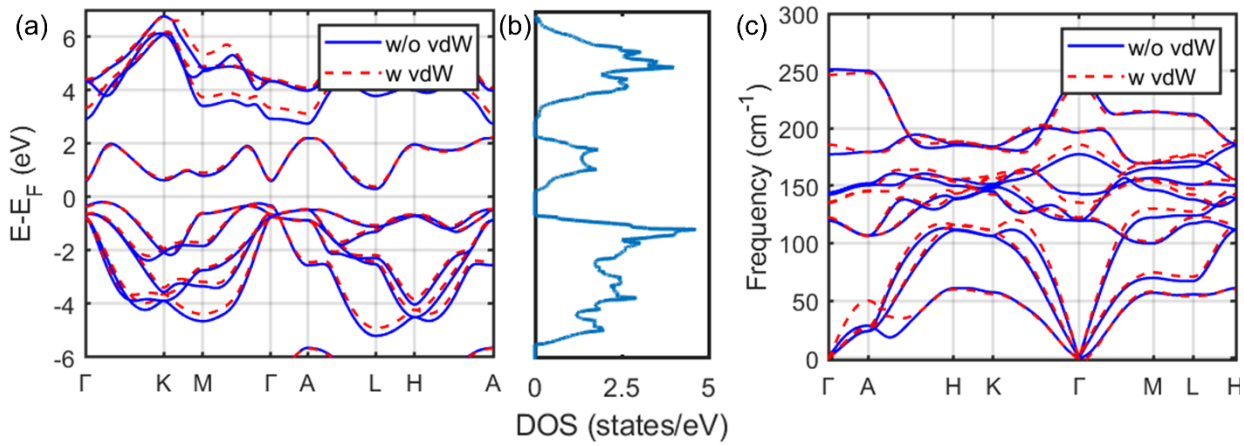

Figure 1. a) Electronic Band structure, b) Electronic density of states (DOS), c) Phonon dispersion of bulk $SnSe_2$ with and without van der Waals interaction. High symmetry points are Γ(0,0,0), K(1/3,1/3,0), M(1/2,0,0), A(0,0,1/2), L(1/2,0,1/2), H(1/3,1/3,1/2)

A recent experimental study on the electronic band structure of $SnSe_2$ single crystals reveals that it is possible to optimize the thermoelectric performance of $SnSe_2$ via electron doping [25]. Thus, to verify the possibility of $SnSe_2$ for commercial applications, doped and undoped $SnSe_2$ single crystals are extensively studied here. In this study, we first reproduce the results of two single-crystal samples reported in the literature. The first one is referred to as the undoped $SnSe_2$ single crystal [25], which was not intentionally doped. However, it shows n-type behavior due to the presence of Se vacancies [51]. Se vacancy results in the average of 2 conduction electrons per vacancy and therefore, $Z = 2$ is used for the calculation of ionized impurity scattering rates of undoped $SnSe_2$ sample. The second one is a doped $SnSe_2$ single crystal referred to as sample Br-SS4 in Pham et al. [30] in which Br is used as the dopant. Each boron atom contributes 1 electron to the conduction band on average and so, $Z = 1$ is used for the calculation of scattering rates. The electrical conductivities and the Seebeck coefficients are calculated using the PERTURBO code based on the BTE under RTA. We study the electron-phonon interactions within the conduction bands. We reproduce the experimental data by using the carrier concentration as a fitting parameter

and minimizing the difference between the theoretical and experimental Seebeck coefficient and the electrical conductivity. This is to build and validate our model.

Figure 2 shows the resulting carrier concentration as well as the experimental values obtained from Hall measurements. It can be seen that obtained carrier concentrations for the doped sample do not coincide with experimental values inferred from Hall measurements. This might partially be because a Hall scattering factor (R_H) of unity was assumed in the measurements but in practice, it can range from 1 to 2. Also, there might be neutral impurities or micro-level defects present in the samples which are not considered in our study. Therefore, the exact carrier densities could be different from the experimentally measured carrier concentrations. Carrier concentration in undoped $SnSe_2$ increases with the temperature, this is expected from a semiconducting sample and is consistent with the measured Hall carrier concentrations. For doped $SnSe_2$, our calculated carrier concentration is off by a factor of around 1.6 compared to Hall measurements which are within the limit of the Hall scattering factor error. First, we started with experimental carrier concentration assuming the Hall scattering factor of unity (R_H=1) to match the experimental Seebeck coefficients but found that the obtained Seebeck coefficients were off by 30-50 μV/K than the actual experimental results as shown in Figure S3. Therefore, we used the carrier concentration as fitting parameters and matched them with the experimental results. We found that an R_H value of 1.6 provides the best results which then results in lower carrier concentration compared to the experimentally reported values. Alternatively, we can explain our lower carrier concentration by the likely formation of Sn vacancies (V_{Sn}^{-2}) as the temperature goes up. [52] These Sn vacancies might provide partial compensation for Se vacancies by forming $V_{Sn}^{-2} - 2Br_{Se}^{+1}$ complexes, which are neutral and electrically inert [52,53].

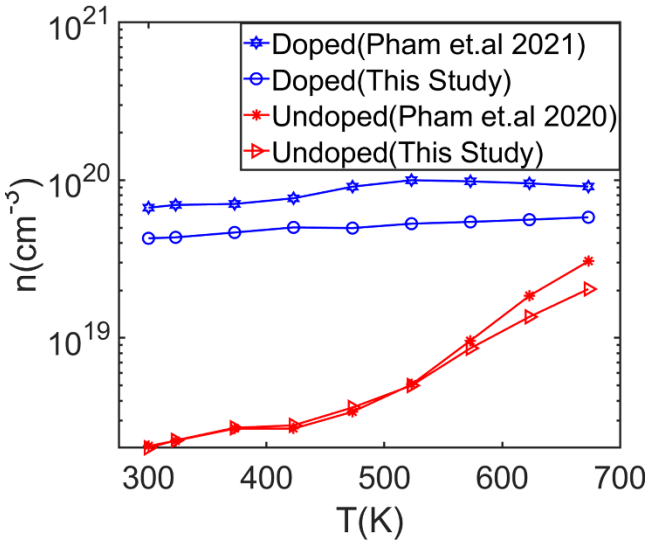

Figure 2. Calculated carrier concentration compared to experimental values obtained from Hall measurements.

Figure 3(a-b) shows the calculated electron-phonon scattering rate with and without the inclusion of vdW interaction, respectively, for different temperatures obtained from the PERTURBO code together with the electronic DOS. The inclusion of vdW interaction slightly increases the electron-phonon scattering rates as shown in Figure 3(b) which is in good agreement with the previous study of Rosul et al [34]. Additionally, the energy dependence of electron-phonon scattering rates follows the electronic DOS energy dependence, since the DOS governs the availability of phase space for electron-phonon scattering.

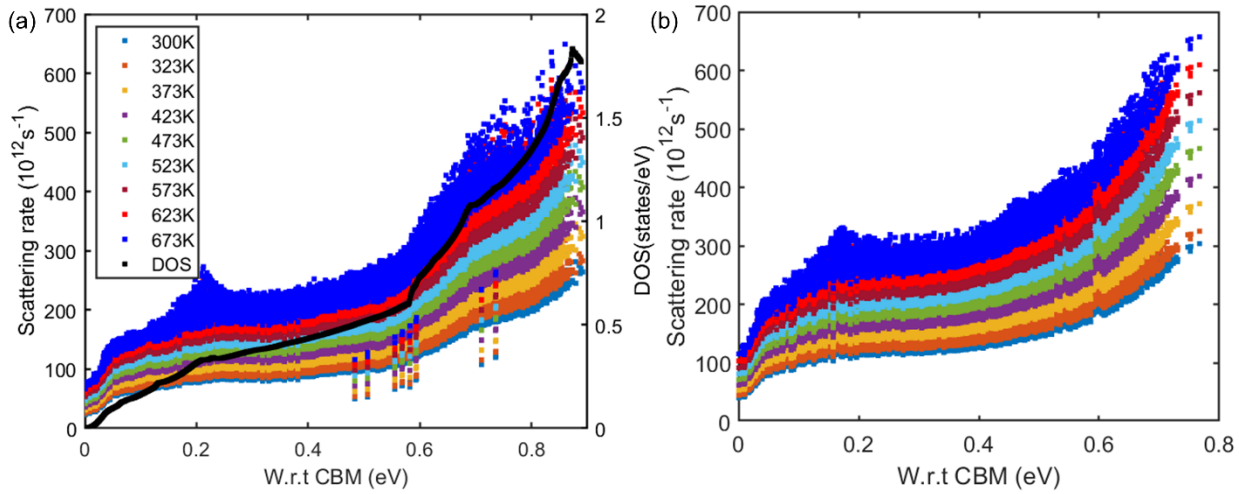

Figure 3. The electron-phonon scattering rates in $SnSe_2$ a) with vdW interaction, b) without vdW interaction for different temperatures with respect to conduction band minimum (CBM).

Figure 4 shows the ionized impurity scattering rates for different carrier concentrations of undoped and doped $SnSe_2$ together with screening length. For undoped $SnSe_2$, the carrier concentration is varied from 2.01×10^{18} cm^{-3} at 300 K to 2.1×10^{19} cm^{-3} at 673 K, and for doped $SnSe_2$, it is varied from 4.82×10^{19} cm^{-3} at 300 K to 5.9×10^{19} cm^{-3} at 673 K. The screening length is calculated based on DOS and Fermi-Dirac distribution. The screening length values range from 1.4 nm to 0.8 nm for undoped $SnSe_2$ and 0.42 nm to 0.515 nm for doped $SnSe_2$. Because of the small values of screening length, ionized impurity scattering is calculated using the modified Brooks-Herring approach considering strongly screened potential. In this approach, the ionized impurity scattering rates strongly depend on screening length (order of 4: L_D^4) compared to carrier concentration (order of 2: N_I^2). For undoped $SnSe_2$, the trend of ionized impurity scattering rates vs temperature can be divided into three parts: i) 300 K-423 K, ii) 473 K-523 K, and c)573 K-673 K. In the range of 300 K-423 K, the ionized impurity scattering rate is mostly dominated by screening length and increases with screening length (Inset Figure (a)). From 473 K to 523 K, screening length decreases by a small margin (1.6nm to 1.45 nm), but carrier concentration increases from 3.5×10^{18} cm^{-3} to

5×10^{18} cm^{-3}. In this range, the ionized impurity scattering rates are governed by carrier concentration and increase with it. Beyond 523 K, screening length abruptly goes down and ionized impurity scattering rates decrease even after increasing carrier concentration. On the other hand, for doped $SnSe_2$, there is no noticeable change in carrier concentration over the whole temperature range, but screening length monotonically increases (Inset Figure 4(b)) with temperature and so, the ionized impurity scattering rates increase with temperature.

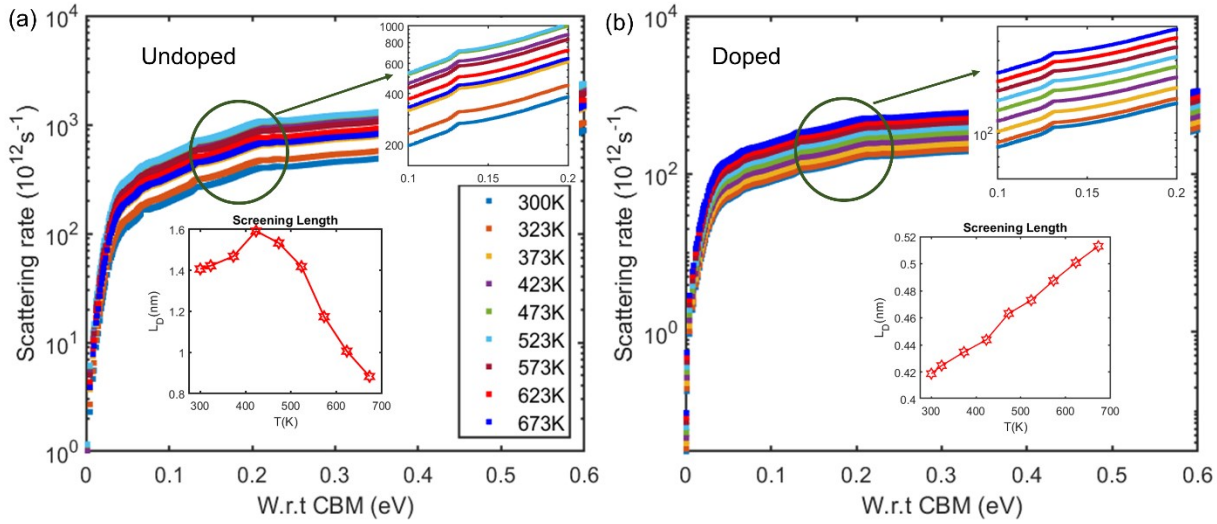

Figure 4. Ionized impurity scattering rates for a) Undoped $SnSe_2$, b) Doped $SnSe_2$ with corresponding screening length.

The thermoelectric properties namely electrical conductivity, Seebeck coefficient, and power factor are calculated using obtained energy-dependent scattering rates as shown in Figures. 5(a-c) and 5(d-f): in-plane and cross-plane for undoped and doped $SnSe_2$, respectively. The cross-plane properties are calculated after the inclusion of vdW interactions in the model. First, we calculate the in-plane and cross-plane electrical conductivities with the inclusion of only electron-phonon scattering rates. Subsequently, ionized impurity scattering rates and vdW interactions are added to the electron-phonon scattering rates. In the undoped sample, electrical conductivity decreases up to 523 K (inset Figure 5(a)) and then increases which is consistent with the ionized impurity

scattering rates. The electrical conductivity of the doped sample is significantly larger than the undoped sample in both in-plane and cross-plane directions. This is mostly due to the increase in the carrier concentration but also due to a lower effective mass of the doped sample. The effective mass of electrons at Γ point is smaller than the L point. At low carrier concentration, electrons occupy only the L-valley but with increasing carrier concentration, Γ valley also starts to be occupied by electrons due to the rise in the chemical potential and electrical conductivity increases significantly. The electrical conductivity of the doped sample decreases continuously with temperature as the electron-phonon scattering and ionized impurity scattering rates increase which confirms the metal-like behavior of the material. Comparing electrical conductivity along both directions, the σ value is lower in the cross-plane direction because of higher effective mass along this direction as shown in Figure 5(d). This denotes the strong anisotropic transport properties of this material. Especially at above 523 K, e.g. for the undoped sample, the σ value along in-plane reaches up to 36 Scm^{-1} whereas, along cross-plane, it is only 9.03 Scm^{-1}.

The effects of electron-phonon, ionized impurity, and vdW interactions on electrical conductivity are shown in Supplementary Information Figure S4. It is expected that the vdW interactions only affect the cross-plane transport direction and not the in-plane ones. Hence, we focused on the inclusion of vdWs only in the cross-plane direction. The inclusion of vdW interactions increases the electron-phonon scattering and we are able to reproduce the experimental electrical conductivity values. In the in-plane direction, we can reproduce the electrical conductivity without vdW interaction. In fact, in the in-plane direction, the inclusion of vdW lowers the electrical conductivity to values below that of the experiment. We acknowledge that this is an artificial effect as we used experimental lattice parameters relaxing only the lattice positions and total stress in the cell is not zero when vdW interaction is added. See supplementary materials for more information.

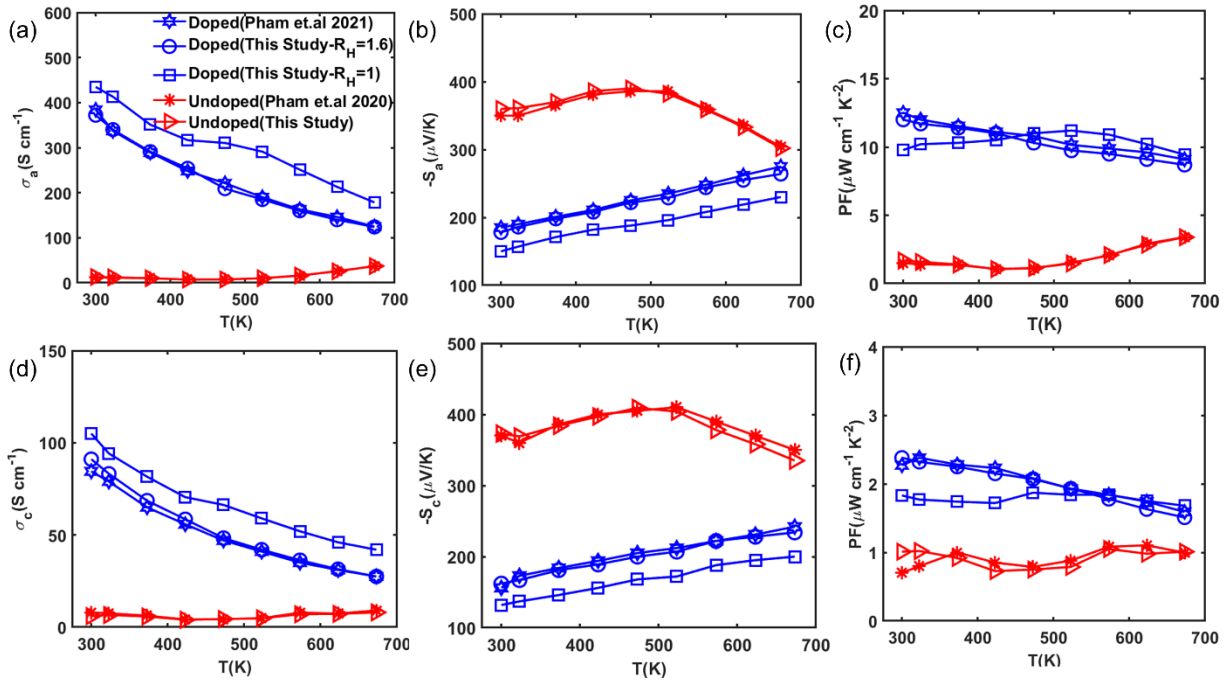

Figure 5. In-plane electrical conductivity, Seebeck coefficients and power factor of undoped and doped $SnSe_2$ (a-c), Cross-plane electrical conductivity, Seebeck coefficients and power factor of undoped and doped $SnSe_2$ (d-f) compared with the literature. The carrier concentration measured experimentally is from Hall data. The data reported for the undoped sample matches that of the experiment using R_H=1. However, the doped sample agrees well with the experiment R_H=1.6 is used.

The Seebeck coefficient along both directions follows a similar trend as shown in Figures 5(b) and 5(e). From room temperature to 523 K, the undoped sample exhibits metallic transport behavior. As expected, Seebeck coefficients slowly increase with the temperature, which is consistent with the decrease in conductivity. Beyond 523 K, the Seebeck coefficient decreases, and the conductivity increases due to the thermal activation of the minority carriers and the bipolar effect. On the contrary, the Seebeck coefficient trend in the doped sample shows metallic-like behavior over the entire temperature range. Owing to the increased carrier concentrations, the Seebeck coefficient of the doped sample is lower than that of the undoped sample. The difference in Seebeck coefficients in each direction is not noticeable but still, there is a slight decrease in Seebeck coefficients along the cross-plane direction. Unlike electrical conductivity, the Seebeck

coefficient remains almost the same even after introducing ionized impurity and vdW interaction. This confirms that Seebeck coefficients are insensitive to the details of relaxation time as shown in Supplementary Information Figure S5.

As mentioned before, we used R_H=1.6 to match the experimental data of the doped sample while we did not need to modify anything for the undoped sample (see Fig. 3). In Fig. 5, we have included the transport calculation results when R_H=1 is used for the doped sample. As shown the results do not match the experiment and hence we modified the carrier concentration.

Combining Seebeck coefficients and electrical conductivities, the thermoelectric power factor (PF) of all samples along both directions is calculated as shown in Figures 5(c) and 5(f). It can be seen that the PF follows the trend of conductivity. The maximum PF along the in-plane for doped (12.5 $\mu W\ m^{-1}\ K^{-2}$) is larger than that along the cross-plane (2.5 $\mu W\ m^{-1}\ K^{-2}$) owing to the relatively large difference in conductivities between the two directions.

Lastly, to report the ZT of $SnSe_2$, lattice thermal conductivity is calculated using Callaway's model and as described in the methodology part. It was reported experimentally that total thermal conductivity is dominated by phonon transport (~95% of total) and so, we limited our calculation to the lattice part of thermal conductivity [30]. Calculated thermal conductivity in comparison with experimentally measured results is shown in Figure 6(a). The parameters used in Callaway's model to fit the experimental values of thermal conductivity are described in Supplementary Information Table S1. The measured thermal conductivity in the cross-plane direction is significantly smaller than the in-plane for all samples because of the weak van der Waals forces along the layers. In this model, we have considered all scattering events and found that impurity scattering dominates at

low temperatures, while the normal three-phonon process and the Umklapp process are the dominant scattering mechanisms at mid and high temperatures.

Finally, using the temperature-dependent thermal conductivity, we have estimated the ZT values in both directions and compared them with the literature [25,30] as shown in Figure 6(b). Although electrical conductivity and Seebeck coefficient show anisotropic behavior, ZT remains almost the same in both directions. This is because the in-plane electrical conductivity and thermal conductivity are both higher than the cross-plane direction and are compensating for each other resulting in the same ZT values.

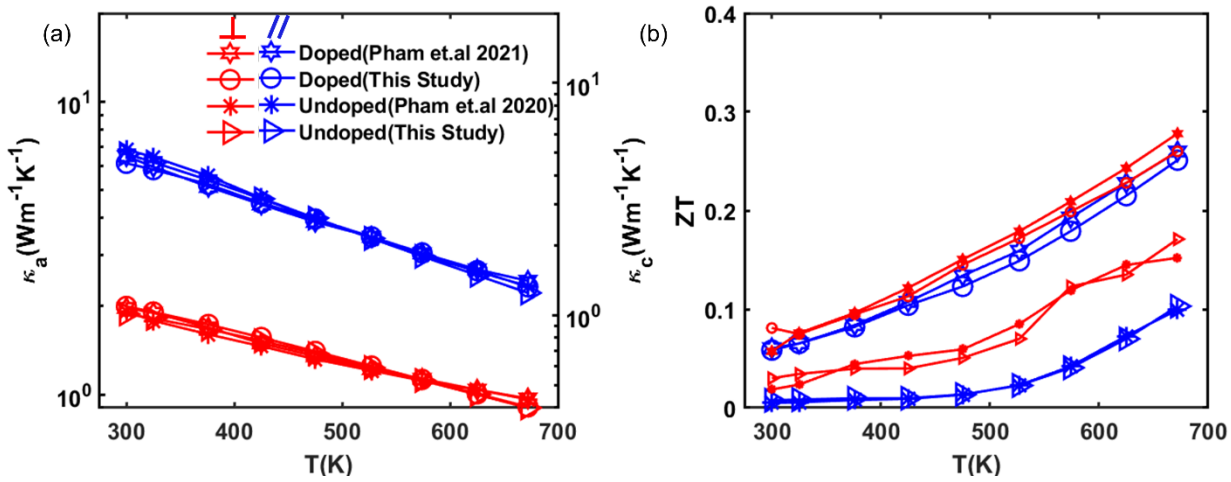

Figure 6. Temperature-dependent thermal conductivity (a) and figure of merit (ZT) (b) along in-plane and cross-plane. Blue color denotes in-plane and red color denotes cross-plane direction.

Finally, after reproducing the experimental data, we use this framework to optimize the PFT (Power factor times temperature) with respect to carrier concentrations and temperature along both directions. At first, we optimize the PFT with respect to carrier concentrations at room temperature as indicated in Figure 7(a). The in-plane PFT reaches a maximum value of 0.398 $Wm^{-1}K^{-1}$ at a carrier concentration of 3.98×10^{19} cm^{-3}. Then, we fix the carrier concentration and vary the

temperature from 300 K to 950 K as shown in Figure 7(b). The in-plane PFT shows a maximum value of 0.49 $Wm^{-1}K^{-1}$ at 523 K. The optimum carrier concentration along the cross-plane direction is 4×10^{19} cm^{-3} which is close to that of the in-plane. The highest cross-plane PFT is 0.185 $Wm^{-1}K^{-1}$ at around 700 K and stays almost constant up to 900K. The ratio PFT_{max}(in-plane)/PFT_{max}(cross-plane) =2.15 denotes strong anisotropy in electrical conductivities and the Seebeck coefficient in our optimization.

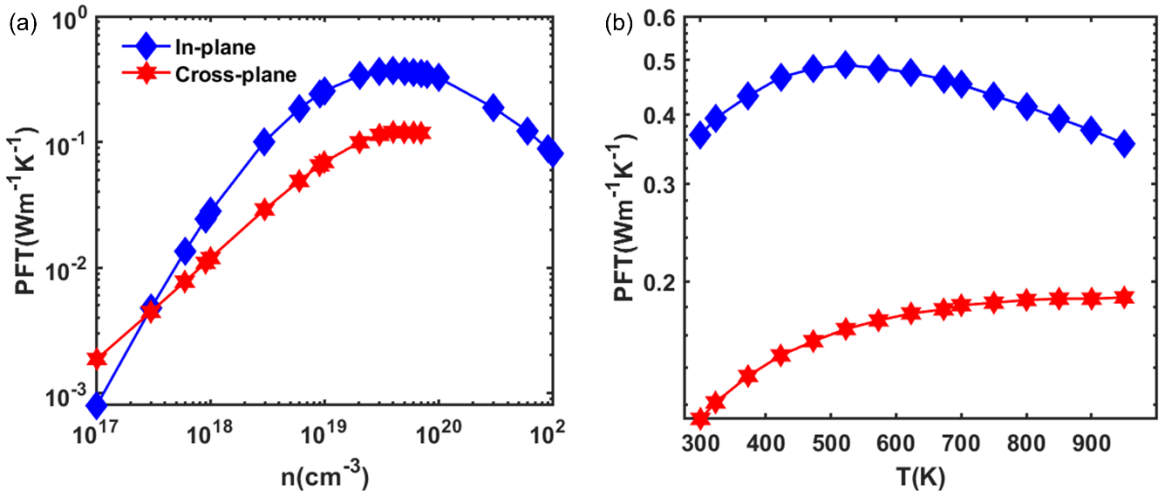

Figure 7: Power factor times temperature at different carrier concentrations (a), power factor time temperature at different temperatures of bulk $SnSe_2$ (b) along both directions.

Next, using our fitted Callaway's model, thermal conductivity is extrapolated up to 950 K in both directions as depicted in Figure 8(a). Ultralow thermal conductivity of around 0.115 $Wm^{-1}K^{-1}$ is found at 950 K in the cross-plane direction which is around 10 times lower than that of in-plane. After obtaining thermal conductivity, the ZT value is calculated and shown in Figure 8(b). Although the PFT value is higher in the in-plane direction, it could not compensate the $\frac{\kappa_a}{\kappa_c}$ ratio. So, the overall ZT value is higher in the cross-plane direction, and it reaches unity at 950 K. Experimentally, the maximum ZT value of 0.56 for single crystal $SnSe_2$ is reported at 673 K along cross-plane [30]. Our optimized ZT value is 0.545 at 673 K which is close to the experimental value

(0.56). Also, the reported ZT values in polycrystalline $SnSe_2$ samples like Ag-$SnSe_2$ (0.4 at 773 K) [54], Br-$SnSe_2$ (0.62 along parallel direction and 0.36 along perpendicular direction at 750K) [55] are in between cross-plane and in-plane boundary as shown in figure 9(b).

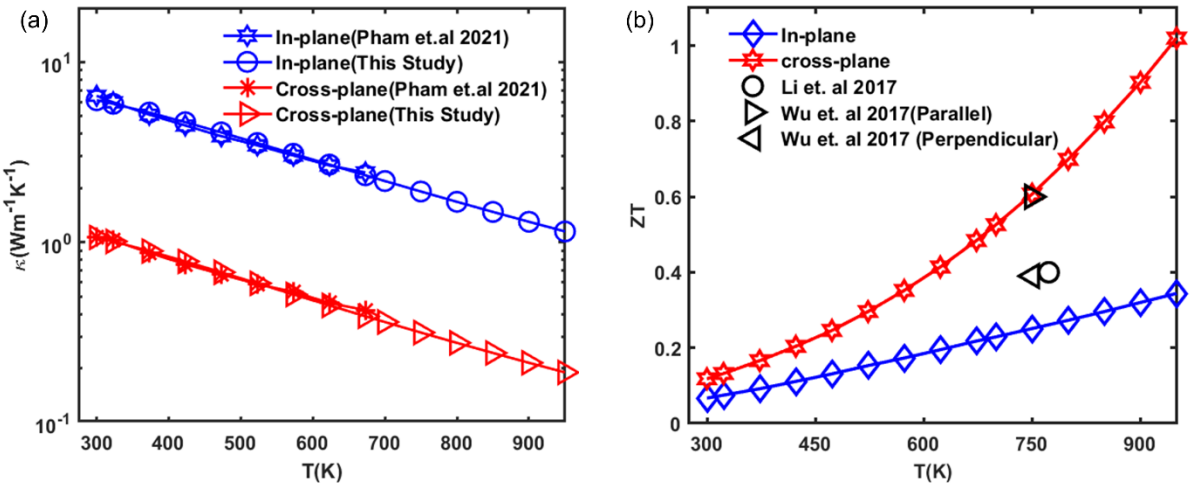

Figure 8: Optimization of temperature-dependent thermal conductivity (a) and figure of merit (ZT) (b) along in-plane and cross-plane directions.

Conclusion:

In conclusion, we have systematically investigated the electronic structure of $SnSe_2$ using density functional theory, evaluated transport properties using BTE under RTA, and used the Callaway model for calculating lattice thermal conductivity. The electron-phonon scattering rates are calculated using the PERTURBO code whereas the ionized impurity scattering rates are obtained using the modified Brooks-Herring approach considering strongly screened coulomb potential. Then, transport calculations were performed using the calculated scattering rates. First, the thermoelectric calculations were carried out for single crystal undoped and doped $SnSe_2$ samples at different carrier concentrations between 300 K to 673 K. The doped sample has a higher thermoelectric power factor compared to the undoped sample. While the in-plane thermoelectric

power factor is higher, the thermoelectric figure of merit is higher in the cross-plane direction because of the ultra-low thermal conductivity due to the very weak interlayer forces, making this material a promising candidate for thermoelectric applications. Our obtained results are in good agreement with experimentally measured values for single crystal samples. This proves the robustness of our developed model which can accurately describe the TE performance of $SnSe_2$ samples. Finally, we optimized the PFT in both directions in terms of different carrier concentrations and found that the optimum carrier concentration is 3.98×10^{19} cm^{-3} which gives the maximum PFT value of 0.49 $Wm^{-1}K^{-1}$ and 0.186 $Wm^{-1}K^{-1}$ along in-plane and cross-plane directions, respectively. Despite having a very high PFT along the in-plane direction, the low κ_c of 0.11 $Wm^{-1}K^{-1}$ leads to a maximum ZT of unity at 950 K along the cross-plane which is 2.85 times larger than that of the in-plane in the doped sample, demonstrating the superior thermoelectric performance along the cross-plane direction. Recently, several studies have reported the potential of Ag or Cu intercalated in layers or embedded in the structure for further improving thermoelectric performance.

Conflicts of interest

There are no conflicts of interest.

Supplementary Information

Additional information related to DFT and Wannier band structure with experimental results, effects of different scattering mechanisms, and Callaway's model fitting parameters is provided.

Acknowledgments

The authors acknowledge discussions with Keivan Esfarjani on the inclusion of vdW interactions. This work is supported by National Science Foundation grant number **2230352**

References:

(1) Gupta, R.; Kumar, N.; Kaur, P.; Bera, C. Theoretical Model for Predicting Thermoelectric Properties of Tin Chalcogenides. *Phys. Chem. Chem. Phys.* **2020**, *22* (34), 18989–19008. https://doi.org/10.1039/d0cp03117h.

(2) Azad, M. A. K.; Rahman, M. H.; Nurani, S. J.; Halim, M. A.; Karim, M. A.; Gulshan, F. Rapid Decolorization of Acid Orange II in Aqueous Solution by Waste Iron Oxide Particles. *J. Mater. Environ. Sci.* **2016**, *7* (3), 685–693.

(3) Xie, L.; He, D.; He, J. SnSe, the Rising Star Thermoelectric Material: A New Paradigm in Atomic Blocks, Building Intriguing Physical Properties. *Mater. Horizons* **2021**, *8* (7), 1847–1865. https://doi.org/10.1039/d1mh00091h.

(4) Liang, W.; Hochbaum, A. I.; Fardy, M.; Rabin, O.; Zhang, M.; Yang, P. Field-Effect Modulation of Seebeck Coefficient in Single PbSe Nanowires. *Nano Lett.* **2009**, *9* (4), 1689–1693. https://doi.org/10.1021/nl900377e.

(5) Pernstich, K. P.; Rössner, B.; Batlogg, B. Field-Effect-Modulated Seebeck Coefficient in Organic Semiconductors. *Nat. Mater.* **2008**, *7* (4), 321–325. https://doi.org/10.1038/nmat2120.

(6) Dresselhaus, M. S.; Chen, G.; Tang, M. Y.; Yang, R.; Lee, H.; Wang, D.; Ren, Z.; Fleurial, J. P.; Gogna, P. New Directions for Low-Dimensional Thermoelectric Materials. *Adv. Mater.* **2007**, *19* (8), 1043–1053. https://doi.org/10.1002/adma.200600527.

(7) Biswas, K.; He, J.; Blum, I. D.; Wu, C.-I.; Hogan, T. P.; Seidman, D. N.; Dravid, V. P.; Kanatzidis, M. G. High-Performance Bulk Thermoelectrics with All-Scale Hierarchical Architectures. *Nature* **2012**, *489* (7416), 414–418. https://doi.org/10.1038/nature11439.

(8) Snyder, G. J.; Toberer, E. S. Complex Thermoelectric Materials. *Nat. Mater.* **2008**, *7* (2), 105–114. https://doi.org/10.1038/nmat2090.

(9) Zebarjadi, M.; Esfarjani, K.; Dresselhaus, M. S.; Ren, Z. F.; Chen, G. Perspectives on Thermoelectrics: From Fundamentals to Device Applications. *Energy Environ. Sci.* **2012**, *5* (1), 5147–5162. https://doi.org/10.1039/C1EE02497C.

(10) Islam, M. A.; Nurani, S. J.; Karim, M. A.; Rahman, A. S. M. S.; Halim, M. A. Dependency of the Band Gap of Electrodeposited Copper Oxide Thin Films on the Concentration of Copper Sulfate (CuSO4.5H2O) and PH in Bath Solution for Photovoltaic Applications. *ICEEE 2015 - 1st Int. Conf. Electr. Electron. Eng.* **2015**, pp. 229–232. https://doi.org/10.1109/CEEE.2015.7428263.

(11) Sales, B. C. Smaller Is Cooler. *Science (80-.).* **2002**, *295* (5558), 1248–1249. https://doi.org/10.1126/science.1069895.

(12) DiSalvo, F. J. Thermoelectric Cooling and Power Generation. *Science (80-.).* **1999**, *285* (5428), 703–706. https://doi.org/10.1126/science.285.5428.703.

(13) Mukherjee, M.; Srivastava, A.; Singh, A. K. Recent Advances in Designing Thermoelectric Materials. *J. Mater. Chem. C* **2022**, *10* (35), 12524–12555. https://doi.org/10.1039/d2tc02448a.

(14) Zebarjadi, M. Electronic Cooling Using Thermoelectric Devices. *Appl. Phys. Lett.* **2015**, *106* (20), 203506. https://doi.org/10.1063/1.4921457.

(15) Adams, M. J.; Verosky, M.; Zebarjadi, M.; Heremans, J. P. Active Peltier Coolers Based on Correlated and Magnon-Drag Metals. *Phys. Rev. Appl.* **2019**, *11* (5), 1. https://doi.org/10.1103/PhysRevApplied.11.054008.

(16) Pham, A. T. Growth and Thermoelectric Properties of SnSe2 Single Crystals. Ph.D.

Dissertation, The Graduate School of the University of Ulsan Department of Physics, University of Ulsan, **2021**.

(17) Shi, X.-L.; Zou, J.; Chen, Z.-G. Advanced Thermoelectric Design: From Materials and Structures to Devices. *Chem. Rev.* **2020**, *120* (15), 7399–7515. https://doi.org/10.1021/acs.chemrev.0c00026.

(18) Riffat, S. B.; Ma, X. Thermoelectrics: A Review of Present and Potential Applications. *Appl. Therm. Eng.* **2003**, *23* (8), 913–935. https://doi.org/10.1016/S1359-4311(03)00012-7.

(19) Finn, P. A.; Asker, C.; Wan, K.; Bilotti, E.; Fenwick, O.; Nielsen, C. B. Thermoelectric Materials: Current Status and Future Challenges. *Front. Electron. Mater*. **2021**, 1, 677845. https://doi.org/10.3389/femat.2021.677845.

(20) Markov, M.; Zebarjadi, M. Thermoelectric Transport in Graphene and 2D Layered Materials. *Nanoscale Microscale Thermophys. Eng.* **2019**, *23* (2), 117–127. https://doi.org/10.1080/15567265.2018.1520762.

(21) Duan, J.; Wang, X.; Lai, X.; Li, G.; Watanabe, K.; Taniguchi, T.; Zebarjadi, M.; Andrei, E. Y. High Thermoelectricpower Factor in Graphene/HBN Devices. *Proc. Natl. Acad. Sci.* **2016**, *113* (50), 14272–14276. https://doi.org/10.1073/pnas.1615913113.

(22) Brixner, L. H. Preparation and Properties of the Single Crystalline AB2-Type Selenides and Tellurides of Niobium, Tantalum, Molybdenum and Tungsten. *J. Inorg. Nucl. Chem.* **1962**, *24* (3), 257–263. https://doi.org/https://doi.org/10.1016/0022-1902(62)80178-X.

(23) Revolinsky, E.; Beerntsen, D. Electrical Properties of the MoTe2−WTe2 and MoSe2−WSe2 Systems. *J. Appl. Phys.* **1964**, *35* (7), 2086–2089. https://doi.org/10.1063/1.1702795.

(24) Mavrokefalos, A.; Lin, Q.; Beekman, M.; Seol, J. H.; Lee, Y. J.; Kong, H.; Pettes, M. T.; Johnson, D. C.; Shi, L. In-Plane Thermal and Thermoelectric Properties of Misfit-Layered [(PbSe)0.99]x(WSe2)x Superlattice Thin Films. *Appl. Phys. Lett.* **2010**, *96* (18), 181908. https://doi.org/10.1063/1.3428577.

(25) Pham, A. T.; Vu, T. H.; Cheng, C.; Trinh, T. L.; Lee, J. E.; Ryu, H.; Hwang, C.; Mo, S. K.; Kim, J.; Zhao, L. D.; Duong, A. T.; Cho, S. High-Quality SnSe2single Crystals: Electronic and Thermoelectric Properties. *ACS Appl. Energy Mater.* **2020**, *3* (11), 10787–10792. https://doi.org/10.1021/acsaem.0c01846.

(26) Shi, W.; Gao, M.; Wei, J.; Gao, J.; Fan, C.; Ashalley, E.; Li, H.; Wang, Z. Tin Selenide (SnSe): Growth, Properties, and Applications. *Adv. Sci. (Weinheim, Baden-Wurttemberg, Ger.* **2018**, *5* (4), 1700602. https://doi.org/10.1002/advs.201700602.

(27) Madsen, G. K. H.; Singh, D. J. BoltzTraP. A Code for Calculating Band-Structure Dependent Quantities. *Comput. Phys. Commun.* **2006**, *175* (1), 67–71. https://doi.org/https://doi.org/10.1016/j.cpc.2006.03.007.

(28) Sun, B. Z.; Ma, Z.; He, C.; Wu, K. Anisotropic Thermoelectric Properties of Layered Compounds in SnX2 (X = S, Se): A Promising Thermoelectric Material. *Phys. Chem. Chem. Phys.* **2015**, *17* (44), 29844–29853. https://doi.org/10.1039/c5cp03700j.

(29) Ding, Y.; Xiao, B.; Tang, G.; Hong, J. Transport Properties and High Thermopower of SnSe2: A Full Ab-Initio Investigation. *J. Phys. Chem. C* **2017**, *121* (1), 225–236. https://doi.org/10.1021/acs.jpcc.6b11467.

(30) Pham, A. T.; Vu, T. H.; Nguyen, Q. V.; Vu, M. T.; Park, J. H.; Park, S. D.; Cho, S. Br-Doped n-Type SnSe2: Single-Crystal Growth and Thermoelectric Properties. *ACS Appl. Energy Mater.* **2021**, *4* (3), 2908–2913. https://doi.org/10.1021/acsaem.1c00278.

(31) Cahill, D. G.; Watson, S. K.; Pohl, R. O. Lower Limit to the Thermal Conductivity of Disordered Crystals. *Phys. Rev. B* **1992**, *46* (10), 6131–6140. https://doi.org/10.1103/PhysRevB.46.6131.

(32) Wang, H.; Gao, Y.; Liu, G. Anisotropic Phonon Transport and Lattice Thermal Conductivities in Tin Dichalcogenides SnS2 and SnSe2. *RSC Adv.* **2017**, *7* (14), 8098–8105. https://doi.org/10.1039/c6ra27761f.

(33) Saeed, Y.; Kachmar, A.; Carignano, M. A. First-Principles Study of the Transport Properties in Bulk and Monolayer MX3 (M = Ti, Zr, Hf and X = S, Se) Compounds. *J. Phys. Chem. C* **2017**, *121* (3), 1399–1403. https://doi.org/10.1021/acs.jpcc.6b08067.

(34) Rosul, M. G.; Zebarjadi, M. Effect of Electron–Phonon Interaction and Ionized Impurity Scattering on the Room-Temperature Thermoelectric Properties of Bulk MoSe2. *J. Phys. Chem. C* **2022**, *126* (35), 15011–15018. https://doi.org/10.1021/acs.jpcc.2c03782.

(35) Lundstrom, M. Fundamentals of Carrier Transport, 2nd Edn. *Meas. Sci. Technol.* **2002**, *13* (2), 230. https://doi.org/10.1088/0957-0233/13/2/703.

(36) Callaway, J. Model for Lattice Thermal Conductivity at Low Temperatures. *Phys. Rev.* **1959**, *113* (4), 1046–1051. https://doi.org/10.1103/PhysRev.113.1046.

(37) Agrawal, B. K.; Verma, G. ~S. Lattice Thermal Conductivity at Low Temperatures. *Phys. Rev.* **1962**, *126* (1), 24–29. https://doi.org/10.1103/PhysRev.126.24.

(38) Manou, P.; Kalomiros, J. A.; Anagnostopoulos, A. N.; Kambas, K. Optical Properties of SnSe2 Single Crystals. *Mater. Res. Bull.* **1996**, *31* (11), 1407–1415. https://doi.org/10.1016/0025-5408(96)00125-0.

(39) Giannozzi, P.; Baroni, S.; Bonini, N.; Calandra, M.; Car, R.; Cavazzoni, C.; Ceresoli, D.; Chiarotti, G. L.; Cococcioni, M.; Dabo, I., et al. QUANTUM ESPRESSO: A Modular and

Open-Source Software Project for Quantum Simulations of Materials. *J. Phys. Condens. Matter* **2009**, *21* (39), 395502. https://doi.org/10.1088/0953-8984/21/39/395502.

(40) Troullier, N.; Martins, J. L. Efficient Pseudopotentials for Plane-Wave Calculations. *Phys. Rev. B* **1991**, *43* (3), 1993–2006. https://doi.org/10.1103/PhysRevB.43.1993.

(41) Perdew, J. P.; Zunger, A. Self-Interaction Correction to Density-Functional Approximations for Many-Electron Systems. *Phys. Rev. B* **1981**, *23* (10), 5048–5079. https://doi.org/10.1103/PhysRevB.23.5048.

(42) Thonhauser, T.; Cooper, V. R.; Li, S.; Puzder, A.; Hyldgaard, P.; Langreth, D. C. Van Der Waals Density Functional: Self-Consistent Potential and the Nature of the van Der Waals Bond. *Phys. Rev. B* **2007**, *76* (12), 125112. https://doi.org/10.1103/PhysRevB.76.125112.

(43) Jiang, H.; Yang, W. Conjugate-Gradient Optimization Method for Orbital-Free Density Functional Calculations. *J. Chem. Phys.* **2004**, *121* (5), 2030–2036. https://doi.org/10.1063/1.1768163.

(44) Byrd, R. H.; Nocedal, J.; Yuan, Y.-X. Global Convergence of a Class of Quasi-Newton Methods on Convex Problems. *SIAM J. Numer. Anal.* **1987**, *24* (5), 1171–1190.

(45) Zhou, J. J.; Park, J.; Lu, I. Te; Maliyov, I.; Tong, X.; Bernardi, M. PERTURBO: A Software Package for Ab Initio Electron–Phonon Interactions, Charge Transport and Ultrafast Dynamics. *Comput. Phys. Commun.* **2021**, *264*, 107970. https://doi.org/10.1016/j.cpc.2021.107970.

(46) Giustino, F.; Cohen, M. L.; Louie, S. G. Electron-Phonon Interaction Using Wannier Functions. *Phys. Rev. B* **2007**, *76* (16), 165108. https://doi.org/10.1103/PhysRevB.76.165108.

(47) Marzari, N.; Mostofi, A. A.; Yates, J. R.; Souza, I.; Vanderbilt, D. Maximally Localized

Wannier Functions: Theory and Applications. *Rev. Mod. Phys.* **2012**, *84* (4), 1419–1475. https://doi.org/10.1103/RevModPhys.84.1419.

(48) Gonzalez, J. M.; Oleynik, I. I. Layer-Dependent Properties of SnS2 and SnSe2 Two-Dimensional Materials. *Phys. Rev. B* **2016**, *94* (12), 125443. https://doi.org/10.1103/PhysRevB.94.125443.

(49) Bilc, D. I.; Benea, D.; Pop, V.; Ghosez, P.; Verstraete, M. J. Electronic and Thermoelectric Properties of Transition-Metal Dichalcogenides. *J. Phys. Chem. C* **2021**, *125* (49), 27084–27097. https://doi.org/10.1021/acs.jpcc.1c07088.

(50) Harbec, J. Y.; Powell, B. M.; Jandl, S. Lattice Dynamics of SnSe2. *Phys. Rev. B* **1983**, *28* (12), 7009–7013. https://doi.org/10.1103/PhysRevB.28.7009.

(51) Heo, S. H.; Baek, S.; Shin, T. J.; Son, J. S. Fabrication of High-Performance SnSe2thermoelectric Thin Films with Preferred Crystallographic Orientation. *Appl. Phys. Lett.* **2022**, *120* (2), 023901. https://doi.org/10.1063/5.0076036.

(52) Chaves, A. S.; Larson, D. T.; Kaxiras, E.; Antonelli, A. Microscopic Origin of the High Thermoelectric Figure of Merit of -Doped SnSe. *Phys. Rev. B* **2021**, *104* (11), 1–11. https://doi.org/10.1103/PhysRevB.104.115204.

(53) Zhou, Y.; Li, W.; Wu, M.; Zhao, L.-D.; He, J.; Wei, S.-H.; Huang, L. Influence of Defects on the Thermoelectricity in SnSe: A Comprehensive Theoretical Study. *Phys. Rev. B* **2018**, *97* (24), 245202. https://doi.org/10.1103/PhysRevB.97.245202.

(54) Li, F.; Zheng, Z.; Li, Y.; Wang, W.; Li, J. F.; Li, B.; Zhong, A.; Luo, J.; Fan, P. Ag-Doped SnSe2 as a Promising Mid-Temperature Thermoelectric Material. *J. Mater. Sci.* **2017**, *52* (17), 10506–10516. https://doi.org/10.1007/s10853-017-1238-8.

(55) Wu, Y.; Li, W.; Faghaninia, A.; Chen, Z.; Li, J.; Zhang, X.; Gao, B.; Lin, S.; Zhou, B.;

Jain, A.; Pei, Y. Promising Thermoelectric Performance in van Der Waals Layered SnSe2. *Mater. Today Phys.* **2017**, *3*, 127–136. https://doi.org/10.1016/j.mtphys.2017.10.001.

Table of Contents Graphics